Hot Hole Transfer at Plasmonic Semiconductor/Semiconductor Interface

ARTICLE

Hot Hole Transfer at Plasmonic Semiconductor/Semiconductor Interface

Mario Gutiérrez,[a] Zichao Lian,[b] Boiko Cohen,*[a] Masanori Sakamoto*[b], and Abderrazzak Douhal*[a]

Localized surface plasmon resonance (LSPR)-induced hot-carrier transfer provides an attractive alternative for light-harvesting using the full solar spectrum. The defect mediated hot carrier transfer is identical in the plasmonic semiconductor/semiconductor interface and can overcome the low efficiency of plasmonic energy conversion thus boosting the efficient IR-light to energy conversion. Here, using femtosecond transient absorption (TA) measurements, we directly observed the ultrafast non-radiative carrier dynamics of LSPR-driven hot holes created in a CuS nanocrystals (NCs) and CuS/CdS hetero nanocrystals (HNCs). We demonstrate that in the CuS NCs, the relaxation dynamics follows a multiple relaxation pathways. Two trap states are populated by the LSPR-induced hot holes in times (100 – 500 fs) that efficiently compete with the conventional LSPR mechanism (250 fs). The trapped hot holes intrinsically relax in 20 - 40 ps and then decay in 80 ns and 700 ns. In the CuS/CdS HNCs, once the CuS trap states have been populated by the LSPR-generated hot holes, the holes transfer through plasmon induced transit hole transfer (PITCT) in 200 - 300 ps to the CdS acceptor phase and relax in 1 - 8 and 40 – 50 μs. The LSPR-recovery shows weak excitation wavelength and fluence dependence, while the dynamics of the trap states remains largely unaffected. The direct observation of formation and decay processes of trap states and hole transfer from trap state provides an important insight into controlling the LSPR-induced relaxation of degenerated semiconductors.

Introduction

Localized surface plasmon resonance (LSPR)-induced carrier transfer holds a key to achieve a paradigm shift in both scientific fields regarding light and solar-energy industry.[1-20] The LSPR band can be tuned over a broad spectral range by modifying the properties of the plasmonic materials such as carrier density,[14, 21-24] crystal structure and morphology,[25, 26] allowing solar energy utilization from the ultraviolet (UV) to infrared (IR) spectral regions.[2, 8, 26-28] However, the low conversion efficiency due to ultrafast relaxation of the LSPR-induced hot carriers and the efficient charge recombination have been major drawbacks of LSPR-induced energy conversion. More specifically, the hot carrier transfer competes with the ultrafast relaxation processes via carrier scattering with timescales of just hundreds of femtoseconds.[4, 7, 29, 30] Therefore, it is difficult to achieve sufficient extraction of energy from LSPR materials for practical applications for energy conversion from the kinetic perspective.

LSPR materials based on semiconductor compounds, such as the copper chalcogenide nanocrystals, poses excellent tunable hole-based LSPR absorption in the near-IR (NIR) region.[6, 20, 21, 23, 24, 31-35] The relaxation of plasmonic copper chalcogenide nanocrystals in combination with their unique carrier-trapping mediated transfer, have boosted their employment as efficient IR-responsive photocatalysts.[20, 31, 36] The carrier trapping process can compete efficiently with the ultrafast relaxation of the generated hot carriers in LSPR materials. For heterostructured nanocrystals (HNCs) composed of plasmonic copper sulfide (CuS) phase and another semiconductor phase (i.e. acceptor phase), trap-mediated hole transfer (plasmon induced transit hole transfer, PITCT) was demonstrated to provide efficient IR-induced catalytic activity.[1, 20] In PITCT, a two-step mechanism is suggested where the first step is the trapping of the LSPR-generated hot carriers in the CuS, which is then followed by transfer of the trapped carriers to the acceptor phase (**Scheme S1**). PITCT occurs in conjunction with the conventional tunneling mechanism, where only the hot holes generated within the region defined by the heterointerface (p–n heterojunction) of the HNCs can participate effectively in interfacial hole transfer. Elucidation of this PITCT-related carrier transport mechanism would pave the way for the highly efficient plasmonic energy conversion. The better understanding of the behavior of hot holes in plasmonic materials, which has remained an ambiguous subject regardless of the unmistakable importance of the development of LSPR-induced carrier transfer materials, will undoubtedly open novel paths for the development of efficient IR-LSPR-responsive materials for varieties of photonic applications. However, important questions still need to be addressed adequately, such as how the heterosurface geometry, its location and the type of environment affect the efficiency of PITCT. For example, in the seminal work describing PITCT the authors studied the PITCT in a system where the heterosurface was formed between CdS nanocrystals on the surface of the CuS nanodisks, but

[a.] *Departamento de Química Física, Facultad de Ciencias Ambientales y Bioquímica, and INAMOL, Universidad de Castilla-La Mancha, Avenida Carlos III, S/N, 45071 Toledo, Spain.*
[b.] *Institute for Chemical Research, Kyoto University, Gokasho, Uji, Kyoto 611-0011, Japan.*
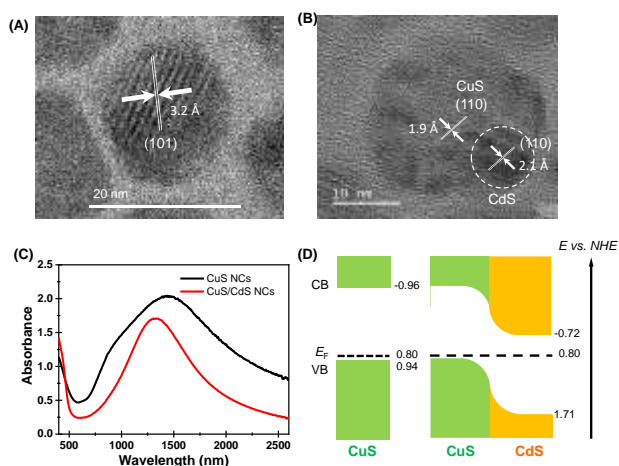
no systematic investigation was performed on the dependence of this process on the size and the location of the CdS phase.[1] On the other hand, the majority of the reported studies were realized in a liquid phase,[1, 19, 31, 36] which do not provide an answer whether the same mechanisms are operational in the solid state, where a significant part of gas phase photocatalytic reactions take place (e.g. photocatalytic CO_2 reduction to solar fuels, oxidation of volatile organic compounds, etc.).[37]

Herein, we elucidated the LSPR-induced behavior of hot holes in CuS NCs and CuS/CdS HNCs using time-resolved optical spectroscopy probing from the visible to NIR spectral region in solid thin film in absence of solvent. Femtosecond TA experiments allow direct observation of the ultrafast carrier dynamics in LSPR-excited CuS NCs or CuS/CdS HNCs. From the detailed investigation of the ultrafast dynamics of LSPR-excited CuS NCs, we discovered that the unique relaxation process transits the two major trap states involved in the LSPR-induced relaxation in addition to the conventional decay of LSPR. Briefly, the trapping times of hot-holes range between 100 and 400 fs, followed by an intrinsic relaxation in 20–40 ps, from where they deactivate in 80 ns (shallow trap states) and 700 ns (deep trap states). Furthermore, the LSPR-induced hole transfer from CuS to CdS acceptor phase (in 200-300 ps) indicated an efficient PITCT. Laser flash photolysis experiments showed two new time components for CuS/CdS HNCs of 1 - 8 and 40 - 50 μs that are assigned to the CdS trap states. The longer-lived relaxation of holes in the CuS/CdS HNCs, because of their transfer to the CdS acceptor phase and the subsequent relaxation from different trap states, offers a unique opportunity for developing more efficient photonic devices. Because the ultrafast relaxation of hot carrier is a major drawback of all plasmonic energy conversion systems, the mechanism studied here should change the conventional consensus regarding LSPR-induced energy conversion due to the overwhelming advantage of high energy conversion efficiency. Additionally, and opposite to most of the reports, the results presented here are on solid-state (thin film) samples, opening a novel avenue fo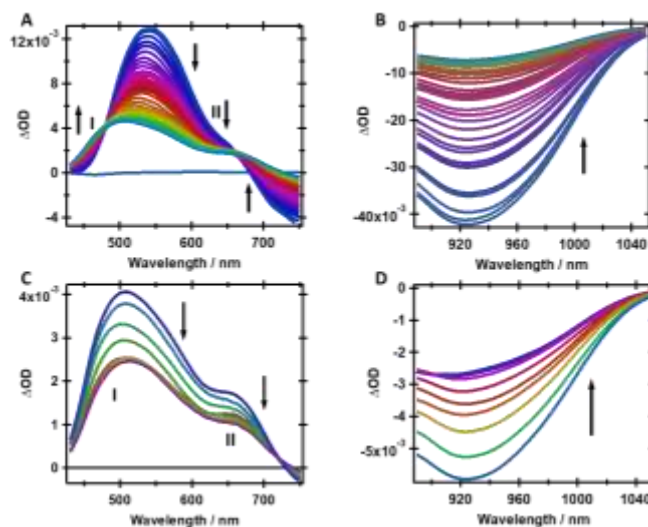r further development of solid-state LSPR-materials, that might boost the improvement of photonics related applications, such as solid-state solar energy conversion or photocatalysis.

Results and Discussion

The hexagonal plate shaped CuS NCs (size: 16.3±1.5 nm; thickness: 5.7±1.1 nm) were synthesized by the previously reported method (**Figure 1A and S1**).[1] We obtained CdS/CuS HNCs via seed-mediated synthesis using hexagonal plate-shaped CuS NCs as seeds (see Methods). The high-resolution transmission electron microscope (HR-TEM) images of CuS NCs and CuS/CdS HNCs are shown in **Figure 1A, B and S2**. The different fringes corresponding to CdS (110) and cv-CuS (110) lattices suggest that the CdS satellite was attached on the edge of CuS disk. In the case of CuS/CdS HNCs, the image shows CdS satellites of 9 nm in size that were deposited on the edge regions of the CuS NCs (**Figure 1B**). We have also characterized the structure of the CuS and CuS/CdS HNCs powder X-ray diffraction (PXRD) (**Figure S3**). The patterns show that the CdS/CuS HNCs were composed of hexagonal covellite CuS (*cv*-CuS, JCPDS no 00-006-0464) and wurtzite CdS (*w*-CdS, JCPDS no. 00-041-1049) phases. The transparent and green uniform films were fabricated by spin coating on glass substrate using ethylene diamine (EDA) or ethanedithiol (EDT) as binder molecules. These binder molecules exchange the protecting ligand of NCs and connect them reinforcing the resulting film. We have selected these two compounds as binders based on their intrinsic properties affecting the band structure of NCs. EDT is known for enhancing the p-type behaviour of semiconductive NCs, while EDA promotes the n-type behaviour.[38, 39]

Figure 2. Time evolution of the TA spectra (TAS) of thin films of CuS (ethylene diamine, EDA) NCs in the visible (A) and (C); and in the NIR (B) and (D) spectral regions at short (A and B, 0 – 2 ps) and long (C and D, 2 ps – 1 ns) time delays, following excitation at 1500 nm. The arrows indicate the time evolution from 0 to 2 ps and from 2 ps to 1 ns. The roman numerals I and II indicate the spectral position of trap state A and B, respectively. Red circles indicate the observed isosbestic points. The spectra have been smoothed for clarity of presentation. Note the difference in the ΔOD values between the short and long-time windows.

Figure 1. HR-TEM images of CuS NCs (A) and CuS/CdS HNCs (B), showing lattice fringes of Cu_9S_5, CuS and CdS phases. C) Absorption spectra of the CuS NCs and CuS/CdS HNCs with the solid ligand exchange of ethanedithiol (EDT). D) Energy diagrams of the CuS NCs and CuS/CdS HNCs.[1]

Figure 1C shows the absorption spectra of CuS NCs and CdS/CuS HNCs film. The CuS NCs showed an LSPR peak at 810 and 1442 nm. The absorption peak of CuS NCs in $CHCl_3$ solution is around 1080 nm.[1] The shift in the NCs film suggest that the plasmon coupling induced blue-shift of absorption spectra occurred in the CuS NCs film.[32] On the contrary, the LSPR peak of the CdS/CuS HNCs was red shifted to 1254 nm, which is similar to that observed in the $CHCl_3$ solution phase. This red shift of the LSPR peak might be attributed to the change of different dielectric environment with the existence of CdS phases.[1] The CdS phase surrounding the CuS NCs suppress the stacking between NCs to avoid the plasmon coupling of CuS domain of HNCs. Additionally, the p-type CuS and n-type CdS would form the p-n heterojunction at the interface.[40] Band diagrams of the CuS and CdS NCs (**Figure 1D**) show that the VB edge of the CdS NCs is 0.91 eV lower than the Fermi level of the CuS NCs (E_F), which suggests that the hot holes generated by NIR excitation of LSPR in the CuS phases could obtain sufficient energy to reach the VB of CdS.[1, 40]

Femtosecond Transient Absorption of CuS NCs

Figures 2A and **2C** show the time evolution of the TA spectra (TAS) of CuS NC thin films following excitation at 1500 nm (IRF ~ 80 fs) in the visible spectral region at short ($0 - 2$ ps, **Figure 2A**) and long time-delays (2 ps $- 1$ ns, **Figure 2C**), while **Figure 2B** and **2D** show the same TAS at short and long temporal scales, but in the NIR region. We did not observe significant differences between the TAS of the NCs using EDT or EDA as binder molecules (**Figure 2** and **Figure S4**), which suggests that the relaxation mechanism for the hot holes in the CuS NCs is independent on the used binder molecules. To begin with, the TAS of CuS showed two isosbestic points located at 480 nm and 670 nm at early times ($0 - 2$ ps), and another at 720 nm at longer times (> 2 ps). While the presence of the isosbestic points at early times has been reported previously,[41] the one at 720 nm at longer delays has not been discussed. This point corresponds to the decay of the positive TAS on one hand and the ground state recovery on the other, indicating a common decay pathway for the hot holes to the relaxed state at longer times.

Notably, the TAS of the CuS NCs in the visible region show multiple positive peaks at 505 nm, 540 nm, 645 nm and 665 nm at different observation times (**Figure 2** and **Figure S4**), contrary to the smooth TAS of the conventional noble metal plasmonic materials derived from the broadening of LSPR.[22, 31] The TAS at early times ($0 - 2$ ps) in the visible spectral range between 400 and 760 nm are composed of two bands centered at 540 nm and 645 nm that in the first $200 - 500$ fs change to two broader bands centered on 505 nm and 665 nm with the vanishing of the bleach LSPR band signal (negative signal at wavelengths > 680 nm). It should be noted that the intensity and the shape of the bands at 645 and 665 nm are strongly affected by the overlap with the blue edge of the LSPR band. Similar behavior of the TAS for CuS NCs in solution has been reported and assigned to the dynamics of the LSPR-induced hot holes and their trapping in deep and shallow trap states (*vide infra*).[1, 36] At longer delays, the broad spectra decay collectively up to 100 ps followed by a constant residual contribution at delays > 1 ns (**Figure 2C**). In the NIR range between 860 and 1070 nm, a single negative band is observed, associated with the recovery of the LSPR due to the relaxation of the

hot holes (**Figure 2B** and **2D**). This band recovers within the first few picoseconds and at longer time delays shows a constant residual contribution in similarity with the TAS behavior in the visible range. The maximum of the ground state recovery NIR band (maximum at 930 nm) is significantly blue-shifted with respect to the steady-state absorption spectrum (1438 nm). The observed blue shift could arise from the overlap of the LSPR-recovery band with the photoinduced absorption at lower energies due to thermalization processes, as previously described for a similar system.[1, 21] It should be noted that the latter has a positive signal but due to limitation in the detector sensitivity in the NIR range we cannot detect it reliably. Thus, the observed time-evolution of the TAS in the visible and NIR spectral regions suggests contribution from different transient species undergoing several parallel processes in the excited state.

The decay profile of the transient species following excitation at 1500 nm at representative probe wavelengths in the visible region (440, 570 and 640 nm) does not fully correspond to the recovery of the LSPR band (900 nm), indicating further that multiple decay processes are involved in the relaxation mechanism of the photo-produced hot holes (**Figure 3**). The dynamics for the same system following excitation at 1000 nm closely resembles the one observed for 1500 nm excitation (**Figures S5** and **S6**).

EDA		a_1 (%)	τ_1 (ps)	a_2 (%)	τ_2 (ps)	a_3 (%)	τ_3 (ps)	a_4 (%)	τ_4 (ns)
CuS	440 nm	100 (-)	0.35	70	40	-	-	30	>1
	570 nm	78	0.32	10	21	-	-	12	>1
	640 nm	36	0.20	30	27	-	-	34	>1
	900 nm	90	0.23	6	23	-	-	4	>1
CuS/CdS	440 nm	100 (-)	0.48	50	28	-	-	50	>1
	570 nm	77	0.32	17	37	-	-	6	>1
	640 nm	62	0.39	27	32	9	315	2	>1
	900 nm	92	0.27	6	34	-	-	2	>1
EDT									
CuS	440 nm	100 (-)	0.34	72	32	-	-	28	>1
	570 nm	78	0.36	10	24	-	-	12	>1
	640 nm	56	0.29	18	35	-	-	26	>1
	900 nm	91	0.20	4	20	-	-	5	>1
CuS/CdS	440 nm	100 (-)	0.31	50	28	-	-	50	>1
	570 nm	79	0.41	13	31	-	-	8	>1
	640 nm	69	0.36	13	35	9	200	9	>1
	900 nm	90	0.27	7	25	-	-	3	>1

Table 1. Fit parameter in terms of time constants (τ_i) and relative contributions (a_i) for the transients of CuS NCs and CuS/CdS HNCs with ethylenediamine (EDA) and ethanedithiol (EDT), probed at the indicated wavelengths. The negative sign indicates a rising component. IRF is 80 fs. The excitation wavelength was 1500 nm.
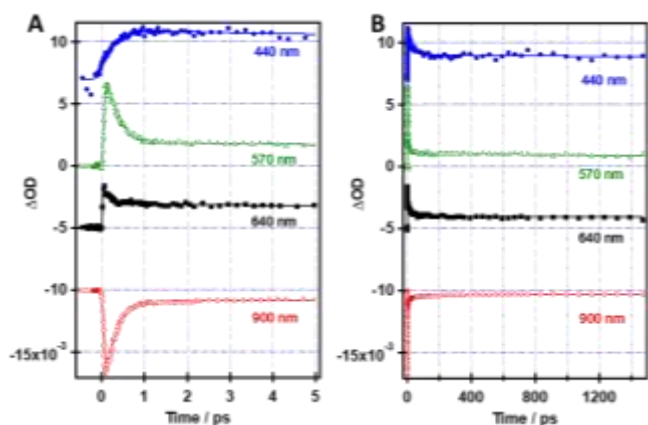
Figure 3: Representative transient decays at selected probe wavelengths (as indicated in the figure) of thin films of CuS (EDA) NCs at short (A) and long (B) time scales following excitation at 1500 nm. The IRF is 80 fs.

Table 1 shows the values of the time constants and the relative contributions obtained from the multi exponential fits to the transient decays of both CuS NCs (EDA and EDT ligands) following excitation at 1500 nm. The transient signal at 570 nm is characterized by a fast decay component of 0.32 ± 0.01 ps, followed by a slower one of 21 ± 2 ps and, finally, a constant contribution that persists for > 1 ns. The transient decay at 440 nm consists of a rising component that has similar value to the decaying one at 570 nm (0.35 ± 0.04 ps), followed by a 40 ± 3 ps component and a constant residual signal at longer delays (> 1 ns). At 640 nm, the TA signal shows a weaker contribution from the fs-component (0.20 ± 0.01, 36%) and decays with 27 ± 4 ps (30%) to a constant offset (> 1 ns, 34%). Finally, the ground state recovery at the NIR part of the spectrum (900 nm) is dominated by an ultrafast component (0.23 ± 0.03 ps, 90%) followed by a 23 ± 3 ps one (6%) and a constant offset (> 1 ns, 4%). It should be noted that the value of the ultrafast component (0.23 ps) for the transient decay at 900 nm is shorter in comparison to the one

observed in the visible part of the spectrum (0.32 ps at 570 nm) indicating different relaxation channels for the excited hot species. Additionally, the fs-decay component in the visible part of the spectra (the transients at 570 and 640 nm) is most probably a combination of two separate components – one that corresponds to the conventional decay of the hot holes back to their relaxed state and the second one corresponding to the trapping of the photoproduced hot holes.

To better characterize the origin of the residual signal in the femtosecond transients, we also interrogated the systems at longer timescales (ns - µs) using laser flash photolysis. The transients collected at 470 nm, 560 nm and 650 nm following LSPR excitation at 1100 nm decay bi-exponentially with time constants of 80 ns and 700 ns (**Figure S7A**). The presence of long-lived components is in agreement with a previous study on CuS NCs that reported a 1.7 µs lifetime.[1] We assign the lifetimes observed in the present work to the decay of the trapped hot holes in deep and shallow trap states. The presence of these long-lived components in all the observation wavelengths suggests a significant overlap of the broad spectral signatures of the associated trap states that is further supported by the femtosecond TAS behavior at long time delays.

Whole picture of CuS relaxation

The TAS behavior of the CuS NCs thin films after optical excitation at the LSPR band (at 1000 and 1500 nm) can be explained by the involvement of three overlapping relaxation processes (**Scheme 1A**). The main one, probed at the bleach recovery band at the NIR, is related to the conventional decay of the hot holes to the relaxed LSPR through a multi-step relaxation mechanism (i.e. plasmon dephasing, hole–hole scattering, hole–phonon coupling, and lattice heat dissipation) with time-constants of 0.23 ps and 23 ps.[1, 22, 31, 36] The other two relaxation processes originate from two different states, State A and State B (Roman numerals I and II in **Figure 2** and **Figure S4**), assigned to trap-mediated decay of the hot holes. The
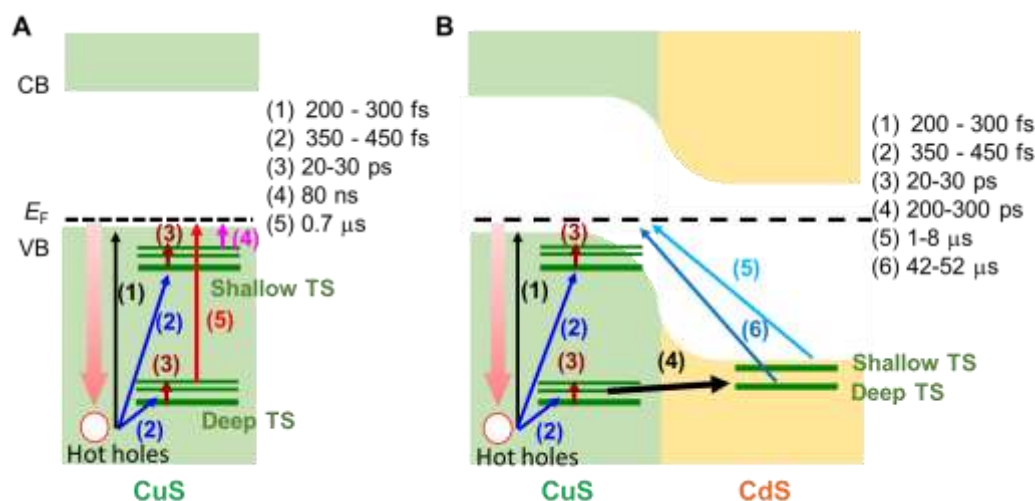

Scheme 1. Schematic Illustration of the carrier dynamics in A) CuS NCs and B) CuS/CdS HNCs after LSPR-band excitation. Three non-radiative relaxation pathways for the LSPR-generated hot holes have been identified. Along with the direct LSPR relaxation, two trap states (State A and State B, see text for details) are populated in times (~350 fs) comparable with the direct LSPR pathway (250 fs). The trapped holes are active to the CdS acceptor phase and are transferred through PITCT in 200 − 300 ps to the CdS trap states that decay in tens of µs.
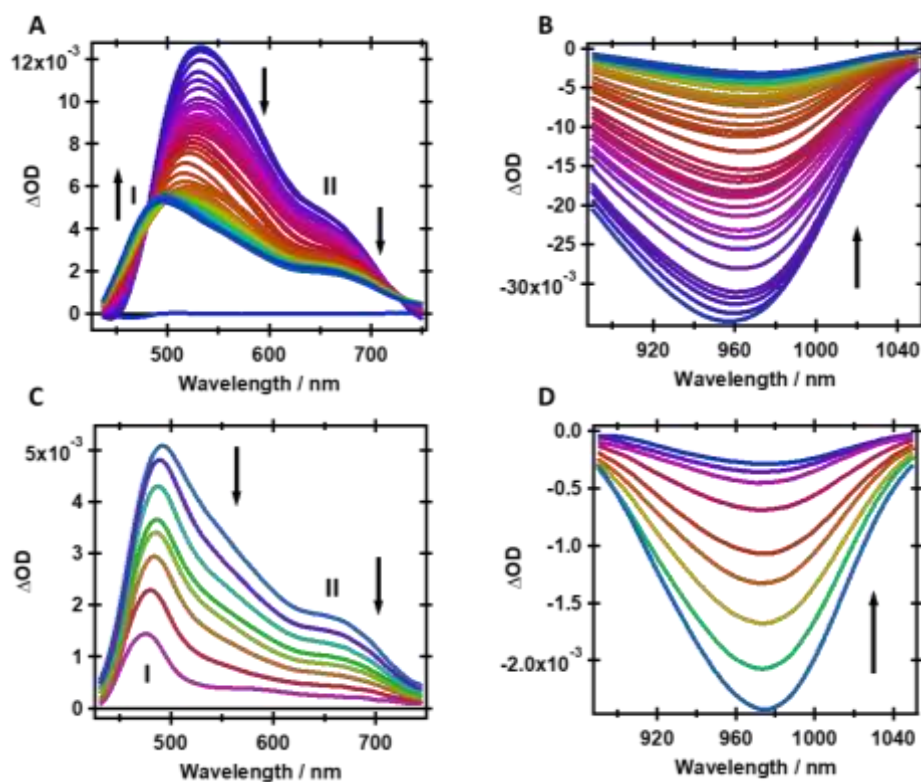
Figure 4. Time evolution of the TAS of thin films of CuS/CdS (EDA) HNCs in the visible (A) and (C); and in the NIR (B) and (D) spectral regions at short (A and B, 0 – 2 ps) and long (C and D, 2 ps – 1 ns) temporal scales, respectively, following excitation at 1500 nm. The arrows indicate the time evolution from 0 to 2 ps and from 2 ps to 1 ns. The roman numerals I and II indicate the spectral position of trap state A and B, respectively. The spectra have been smoothed for clarity of presentation. Note the difference in the ΔOD values between the short and long-time windows.

trap states are likely associated with S atoms that have a Cu deficiency, displacement of Cu, and/or ligands on the surface of CuS NCs.[36] We assign the decay (at 570 nm) and rising (at 440 nm) component with a value of 0.35 ps to the formation of a population of trapped hot holes in the CuS NCs (state A). On the other hand, State B (670 nm) is accessible within the IRF (~ 80 fs) and decays with time constant similar to the one assigned to the relaxation of State A, which suggests that following the initial trapping of the hot holes they undergo intrinsic relaxation within each state (30 – 40 ps). Time constants of 20 – 190 ps have been reported previously for CuS NCs and were assigned to either intrinsic relaxation in the trap states,[41] or charge recombination/relaxation from a shallow trap state close to the valence band edge.[1, 36] Using laser flash photolysis, we resolved the residual contribution in the femtosecond TAS at all the probe wavelengths (80 ns and 700 ns) and assign it to the decay of the trapped hot holes from the trap State A and B to the relaxed state. The trapping of the hot holes, associated with the presence of deep and shallow trap states in the CuS NCs characterized by long relaxation times has been reported previously for CuS NCs in solution.[1, 36, 41] We did not observe significant difference between the reported values of the time constants for the primary steps of the LSPR-hot hole generation and trapping in solution and those observed in the current study for the thin film samples. On the other hand, the times for the relaxation from the trap states decreases notably in absence of solvent. We explain this difference with the

interaction of the molecular oxygen with the surface of the thin film samples, while in the typical inactive-gas-purged solution, the interaction between O_2 and the surface of the CuS would not be observed. Thus, we suggest that the LSPR-induced hot holes in the CuS NCs (EDA and EDT) decay to the relaxed state via the conventional decay channels of LSPR and through hot carrier trapping - mediated decay (States A and B). Scheme 1A illustrates a
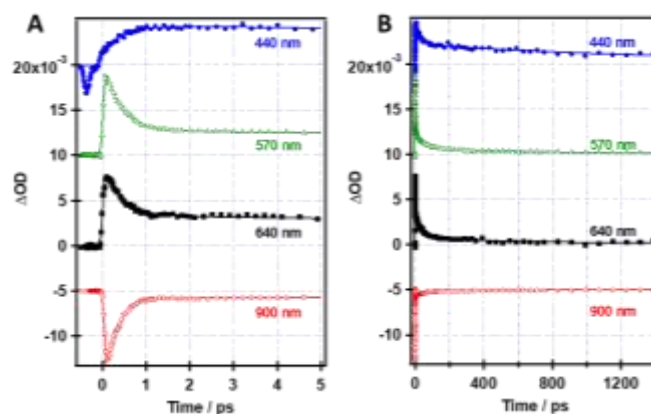
Figure 5. Representative transient decays at selected probe wavelengths (as indicated in the figure) of thin films of CuS/CdS (EDA) HNCs at short (A) and long (B) time scales following excitation at 1500 nm. The IRF is 80 fs.
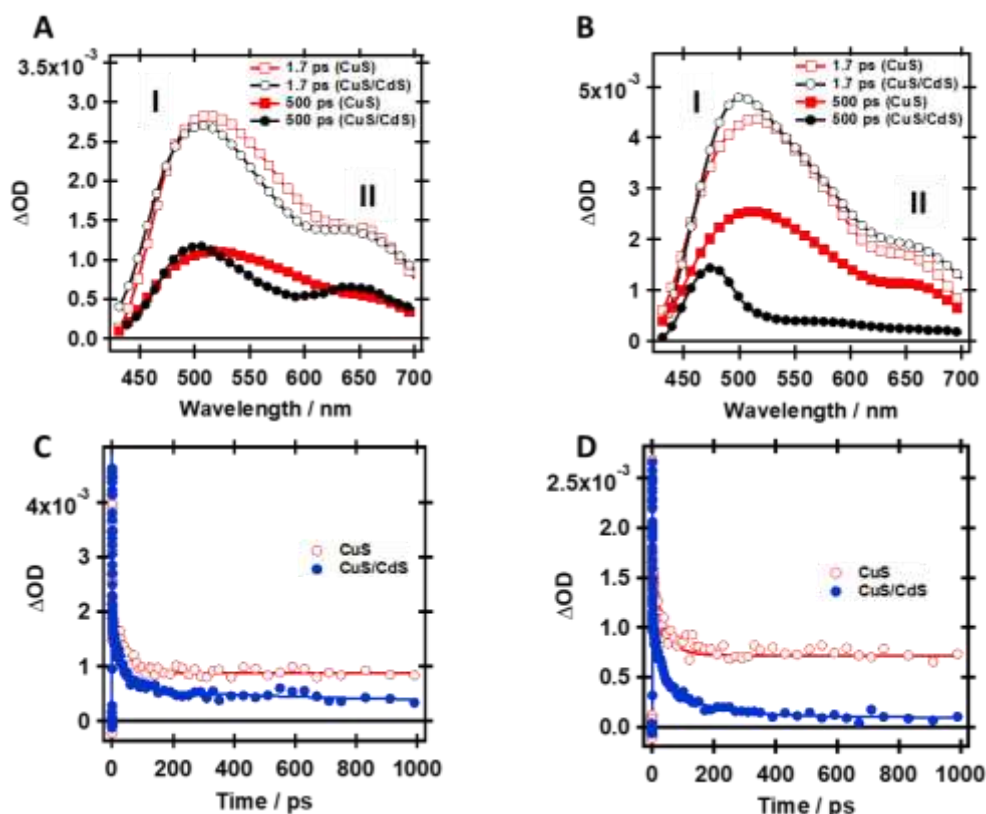
Figure 6. Comparison of the TA spectra A) and B) at short (1.7 ps) and long (500 ps) time delays for the films prepared using EDT and EDA ligands, respectively. C) and D) show a comparison of the decays at 640 nm for the systems under study for films prepared using EDT and EDA ligands, respectively. The roman numerals I and II indicate the spectral position of trap state A and B, respectively. The excitation wavelength was 1500 nm. The IRF is 80 fs.

summary of the hot holes photodynamics in the CuS NCs upon their photoexcitation with 1000 or 1500 nm.

Effect of CdS (acceptor phase)

Next, we studied the TAS of CuS/CdS HNCs following excitation at the LSPR band of the CuS at 1500 nm (**Figure 4 and Figure S8**). The observed TAS of the CuS/CdS HNCs is derived from the excitation of the CuS phase. The time evolution of the TAS at early times (0 – 2 ps) for the CuS/CdS HNCs closely resemble those of the CuS NC thin films (**Figure 4A** and **4B**). Thus, this suggests that the early-time dynamics of the hot holes in the HNCs is dominated by the same competing processes observed for the CuS ones – the conventional LSPR relaxation (NIR bleach recovery, **Figure 4B**) and the trap-mediated decay through States A (460 nm) and B (670 nm). Following the optical excitation at the LSPR band of both the EDA and EDT-based HNCs, the TAS consist of two positive bands at 540 nm and 670 nm (**Figure 4A** and **Figure S8A**). The band at 540 nm decays in the first few hundred fs to give rise to a new, broad band centered at 500 nm. In similarity with the CuS NCs, we assign this new band to a population of trapped hot holes in State A, while State B is populated within the IRF. However, at longer time-delays (2 ps – 1 ns), once the trap states of CuS have been populated by the LSPR-generated hot holes, we observed significant differences in the TAS behavior between the CuS NCs and CuS/CdS HNCs (**Figure 4C** and **4D**). At

longer times, the band at 500 nm shifts further to 470 nm and becomes significantly narrower. This new band decays to constant offset, while the bands at 500 nm, 540 nm and 670 nm decay almost to zero (~2% at 670 nm) for the CuS/CdS (EDA) HNCs (**Figure 4C**) and to weak (~9%) constant contribution for the CuS/CdS (EDT) ones (**Figure S8C**). Similar trend is observed for the LSPR recovery band (NIR, **Figure 4D** and **Figure S8D**), which decays rapidly (within the first 200 fs) to either a weak constant offset or almost to zero, for the CuS/CdS (EDT) and CuS/CdS (EDA) HNCs, respectively.

We analyzed the TA dynamics following excitation at 1500 nm at selected representative probe wavelengths that correspond to the bands associated with the different relaxation processes (**Figure 5A** and **5B**, and **Table 1**). In similarity with the TAS for the crystals without the CdS acceptor phase, the different excitation wavelengths did not produce notable differences in the observed dynamics (**Figures S9** and **S10**). To begin with, the transient at 900 nm (LSPR recovery band) recovers bi-exponentially, with time constants of 0.27 ± 0.03 ps and 34 ± 4 ps. These values are similar to those obtained for the CuS NCs, which indicates that the conventional LSPR relaxation process is unaffected by the CdS hole acceptor phase. The same trend is observed for the relaxation dynamics of State A probed at 440 nm. The transient rises in 0.45 ± 0.05 ps and decays in 50 ± 3 ps to a constant residual offset (> 1 ns) for both CuS/CdS HNCs (EDT and EDA). On the other hand, when the dynamics was probed at 640

nm, the decays were fitted by 3-exponential function giving values of 0.39 ± 0.02 ps, 38 ± 3 ps and 212 ± 15 ps for the CuS/CdS (EDT) HNCs, and 0.43± 0.03 ps, 32 ± 4 ps and 315 ± 20 ps for the CuS/CdS (EDA) ones (**Table 1**). Both transients reach a residual offset but the one for the EDA-based HNCs has a significantly lower contribution at < 3% (**Figure 6**). Thus, in the case of the CuS/CdS HNCs, we suggest that the trapped holes generated in the CuS phase transfer to the CdS valence band via PITCT in 200 − 300 ps. Similar value (177 ps), associated with PITCT from the CuS trap states to CdS acceptor phase has been reported for CuS NCs (diameter of 16 nm) with CdS crystals (3.8 nm) seeded on the surface of the CuS phase.[1]

We also found that the PITCT in our experiments is associated with notable changes in the spectra at longer time delays for both HNCs systems (**Figure 4** and **6**). While the TAS of the CuS NCs at the high energy side of the spectra (430 − 550 nm) are broad and remain largely unchanged even at 1 ns, those of the CuS/CdS HNCs become significantly narrower and shift further to the blue (470 nm), which suggests that the band at 470 nm arises from a population of trapped holes in the CdS phase following efficient PITCT. Additionally, this effect is more pronounced for the HNCs films with the EDA ligands than for the EDT ones, indicating that the PITCT mechanism is more efficient in the CuS/CdS (EDA) system than in the EDT-based one. This difference can be explained in terms of the doping properties of the ligands. These ligands modify the VB or CB position through their electron- or hole – extracting properties.[38, 39, 42] EDT enhances a p-type behavior of semiconductive NCs and can block the flow of electrons causing an upshift of the valence band position as demonstrated for colloidal quantum dot bilayer heterojunction solar cells.[38] On the other hand, EDA promote the n-type behavior that can be oxidized by the holes trapped in the CdS phase, thus making the PITCT more efficient.[39]

The laser flash photolysis experiments for the CuS/CdS HNCs following excitation at the CuS LSPR band (1100 nm) and probing at 470 nm reveal a biexponential decay with time constants of 8 μs and 50 μs for the EDA-based HNC system (**Figure S7B**). These values are significantly larger than the ones assigned to the relaxation of the trapped holes in the CuS NCs. On the other hand, for the EDT-based one, the bi-exponential decay yields time constants of 1 μs and 42 μs (**Figure S7C**). The short time component is similar to the one found for the CuS NCs, while the longer one of 42 μs is comparable to the long component of the EDA-based HNC system. This behavior agrees with the one observed in the TAS experiments, and further demonstrates the different effect of the ligand molecule properties on the PITCT, which is more efficient for the EDA (promoting n-type behavior of CuS) based one. Contrary to the observation for the CuS NC systems, where we could record reliable signal also at 560 nm and 650 nm, for the CuS/CdS HNCs ones we found only a negligible contribution at these wavelengths of observation. This agrees with the TA signal recorded for long time delays, where a very narrow band with a maximum at 470 nm was found. Additionally, a 9.2-μs decay time was reported for the PITCT assisted trapped holes in the CdS phase seeded on the surface of CuS NCs, while a significantly longer decay time (557 μs) was observed for a CuS/CdS HNC system in solution comparable in structure to the one studied here.[1, 20] Thus,

for the EDT and EDA-based CuS/CdS HNCs thin films, we assign the observed time components to the decay of the trapped holes from the CdS deep and shallow trap states following the PITCT from the trap states of the CuS phase, as summarized in **Scheme 1B**. These results further support the interaction with the molecular oxygen affects the carrier dynamics in solid thin film. Additionally, they also demonstrate that the survival times of the trapped holes are sensitive both to the size of the CdS acceptor phase[20] and to the presence of molecular oxygen. On the other hand, the lack of significant dependence of the early time dynamics (the primary steps) related to the relaxation and trapping of the hot holes in the CuS phase, and the mild change in the time for PITCT on the used ligand and heterosurface geometry indicates that while the formed p-n heterojunction favors the transfer of the hot carriers between the two phase, the efficiency of PITCT is predominantly affected by the properties of the ligand.

Excitation wavelength and fluence dependence

Next, we studied the effect of the excitation wavelength on the dynamics of the observed relaxation processes in both the NCs and the HNCs using EDA and EDT binder molecules. We selected two excitation wavelengths within the LSPR band (1000 nm and 1500 nm) and one in the CuS band gap (500 nm). The band gap excitation wavelength was selected to avoid direct excitation of the CdS acceptor phase in the CuS/CdS HNCs (**Figure S11**). When exciting at the band gap (500 nm), it is expected that the decays should arise from the photoinduced electron in the conduction band in addition to the already observed hole dynamics. However, the transients (data not shown) closely resemble the ones collected upon LSPR-band excitation (1000 and 1500 nm), indicating that the signals after band gap excitation are also dominated by the trapped hole absorption with negligible contribution from photoinduced electrons in the conduction band. As noted, little difference is observed also when the excitation wavelength was changed from 1500 nm (0.83 eV) to the more energetic 1000-nm one (1.24 eV). The most notable effect for the transient of both the CuS NCs and CuS/CdS HNCs (EDA and EDT), however, can be observed in the decays associated with the conventional LSPR relaxation process (560 nm and 900 nm, Figures **S5B, S5D, S9B** and **S9D**), where the time constant for the processes associated with the ultrafast relaxation through LPSR dephasing, hole–hole scattering, hole–phonon coupling, changes from 200 fs to 400 fs upon increasing the excitation wavelength energy. Similar increase in the value of the ultrafast component associated with the LSPR-relaxation is observed in the transient of CuS NCs and CuS/CdS HNCs independently of the binder molecule when the excitation pump power was increased from 2 mW to 8 mW (**Figures S12** and **S13**). This behavior suggests that the excitation energy affects predominantly the conventional LSPR relaxation pathway, while the dynamics of the trap-mediated decay channels remains largely unaffected. Finally, because the relaxation dynamics of both the NCs and HNCs remained largely unaffected by the excitation energy and laser fluence, their behavior is most likely not a result of a nonlinear optical phenomenon or a many-body effect.

Conclusions

In this work, we unraveled the unique LSPR-induced relaxation processes of CuS NCs and CuS/CdS HNCs that involve two major trap sites/states of CuS domain in addition to the conventional decay of LSPR (direct). Although the direct decay of the LSPR-induced hot carriers is the dominant relaxation channel that allows non-radiative decay in 250 fs and thermal dissipation in $20 - 50$ ps, we also observed efficient formation (~400 fs), relaxation ($30 - 40$ ps) and decay (80 and 700 ns) processes of the hot holes in two trap states. The dynamics of the CuS/CdS HNCs shows evidence for PITCT ($200 - 300$ ps) that is more efficient in presence of the EDA binder molecules. We find that in the solid thin films, the survival time of the trapped hot carriers is affected by the interactions with the atmospheric molecular oxygen. Excitation power and wavelength dependence studies of both the CuS NCs and the CuS/CdS HNCs show that the conventional LSPR decay channel is weakly dependent on the variation of the excitation energy, while the dynamics of the hot holes in both trap states remains largely unaffected. Thus, the direct observation of formation and decay processes of trap states provide important insight into controlling the LSPR-induced relaxation of degenerated semiconductors. The amount of photogenerated trapped hot carriers can be controlled by the laser fluence, molecular oxygen accessibility and surface protecting ligand on CuS NCs and CuS/CdS HNCs. The mechanism proposed here should support us to change the conventional consensus regarding LSPR-induced energy conversion due to the overwhelming advantage of high energy conversion efficiency.

Methods

Characterization

High-resolution transmission electron microscopy (HR-TEM) characterization was carried out on JEM-2200FS (JEOL) electron microscope at an acceleration voltage of 200kV. The XRD patterns were recorded on a PANalytical Aeris diffractometer, with Cu Kα radiation (λ = 1.542 Å) at 40 kV and 15 mA. Ultraviolet-visible-near-infrared (UV-Vis-NIR) absorption spectra were obtained using a UV–3600 spectrophotometer (Shimadzu).

Synthesis of CuS nanocrystals (NCs) and CdS/CuS hetero nanocrystals (HNCs)

CuS NCs were synthesized according to the previous report.[1] We synthesized CdS/CuS HNCs via seed-mediated synthesis using hexagonal plate-shaped CuS NCs as seeds using the modified method of previously reported CuS/CdS HNCs. A mixed solution of the CuS NCs (0.8 mmol), oleylamine (20 mL), and 1-octadecene (40 mL) was degassed at 150 °C for 30 min. A solution of the Cd precursor [$Cd(S_2CNEt_2)_2$, 200 mg] in oleylamine (8 mL) was prepared under ultrasonication, injected into the above mixed solution under a N_2 atmosphere at a rate of 0.1 mL min^{-1}, and stirred for an additional 30 min. After this time, the obtained product was purified by centrifugation in a chloroform–ethanol (1:1, v/v) mixed solvent and redispersed in chloroform.

Preparation of the CuS or CuS/CdS film

A dense CuS NCs or CuS/CdS HNCs layer was prepared on glass or quartz substrates by layer-by-layer deposition by spin-coating NCs solution (100 mg/mL in octane) and binder molecule solution (ethane dithiol or ethylene diamine, 0.3% v/v in acetonitrile). The thickness of the NCs films was adjusted to give OD of 1.0 at 1000 nm.

TA measurements

The femtosecond TA studies were performed using a chirped pulse amplification (CPA) system. In brief, it consists of a diode-lase (Verdi V6, Coherent) pumped Ti:Sapphire oscillator (CDP systems) that provides the seed pulse (800 nm, 50 fs, 360 mW, 87 MHz) for the CPA system (Legend HE, Coherent). The output of the CPA (800 nm, 3.2W, 1kHz, 35 fs) is split in two parts. The main portion is used to pump a collinear optical parametric amplifier (TOPAS Prime, Positive Light) to give the excitation wavelengths (500, 1000 and 1500 nm). The pump fluence was varied by variable neutral density filter to give values of 2, 4, 6 and 8 mW at the sample. The intensity of the second part of the fundamental beam is attenuated and used to generate the white light continuum in a 3-mm thick sapphire crystal. The spot size of the pump was measured using the razor blade technique to give a value of 320 μm, which gives a ratio of 3:1 with respect to the probe beam.

Flash photolysis

The UV–visible a nanosecond to second laser flash photolysis setup consists of a LKS.60 laser flash photolysis spectrometer (Applied Photophysics), a Vibrant (HE) 355 II laser (Opotek) as a pump pulse source (5 ns time duration), and a 150 W xenon arc lamp as a probe. The signal from optical parametric oscillator (355 nm-pumped by Q-switched Nd/YAG laser, Brilliant, Quantel) at 1100 nm was used for the sample excitation. The probing light transmitted through the sample was dispersed by a monochromator and detected by a UV–visible photomultiplier coupled to a digital oscilloscope (Agilent Infiniium DS08064A, 600 MHz, 4 GSa/s). The pump energy pulse (5 mJ/pulse) was attenuated by a half-waveplate and a polarizer pair.

Conflicts of interest

There are no conflicts to declare.

Acknowledgements

Notes and references

1. Z. Lian, M. Sakamoto, H. Matsunaga, J. J. M. Vequizo, A. Yamakata, M. Haruta, H. Kurata, W. Ota, T. Sato and T. Teranishi, *Nat. Commun.*, 2018, **9**, 2314.
2. K. M. Mayer and J. H. Hafner, *Chem. Rev.*, 2011, **111**, 3828-3857.
3. X. Zhang, Y. L. Chen, R.-S. Liu and D. P. Tsai, *Rep. Progr. Phys.*, 2013, **76**, 046401.
4. C. Clavero, *Nat. Photonics*, 2014, **8**, 95-103.
5. M. L. Brongersma, N. J. Halas and P. Nordlander, *Nat. Nanotechnol.*, 2015, **10**, 25-34.
6. Y. Liu, M. Liu and M. T. Swihart, *J. Phys. Chem. C*, 2017, **121**, 13435-13447.
7. A. Furube and S. Hashimoto, *NPG Asia Mater.*, 2017, **9**, e454-e454.
8. A. Agrawal, S. H. Cho, O. Zandi, S. Ghosh, R. W. Johns and D. J. Milliron, *Chem. Rev.*, 2018, **118**, 3121-3207.
9. P. Baláž, M. Baláž, M. Achimovičová, Z. Bujňáková and E. Dutková, *J. Mater. Sci.*, 2017, **52**, 11851-11890.
10. C. Coughlan, M. Ibáñez, O. Dobrozhan, A. Singh, A. Cabot and K. M. Ryan, *Chem. Rev.*, 2017, **117**, 5865-6109.
11. A. Gellé, T. Jin, L. de la Garza, G. D. Price, L. V. Besteiro and A. Moores, *Chem. Rev.*, 2020, **120**, 986-1041.
12. M. Sakamoto, T. Kawawaki, M. Kimura, T. Yoshinaga, J. J. M. Vequizo, H. Matsunaga, C. S. K. Ranasinghe, A. Yamakata, H. Matsuzaki, A. Furube and T. Teranishi, *Nat. Commun.*, 2019, **10**, 406.
13. C. Zhang, F. Jia, Z. Li, X. Huang and G. Lu, *Nano Research*, 2020, **13**, 3183-3197.
14. Y. Zhao and C. Burda, *Energy Envir. Sci.*, 2012, **5**, 5564-5576.
15. P. Christopher and M. Moskovits, *Annu. Rev. Phys. Chem.*, 2017, **68**, 379-398.
16. J. Pettine and D. J. Nesbitt, *J. Phys. Chem. C*, 2022, **126**, 14767-14780.
17. F.-X. Xiao and B. Liu, *Nanoscale*, 2017, **9**, 17118-17132.
18. F.-X. Xiao and B. Liu, *Adv. Mater. Inter.*, 2018, **5**, 1701098.
19. Z. Zeng, T. Li, Y.-B. Li, X.-C. Dai, M.-H. Huang, Y. He, G. Xiao and F.-X. Xiao, *J. Mater. Chem. A*, 2018, **6**, 24686-24692.
20. Z. Lian, Y. Kobayashi, J. J. M. Vequizo, C. S. K. Ranasinghe, A. Yamakata, T. Nagai, K. Kimoto, K. Kobayashi, K. Tanaka, T. Teranishi and M. Sakamoto, *Nat. Sustain.*, 2022, DOI: 10.1038/s41893-022-00975-9.
21. Y. Xie, L. Carbone, C. Nobile, V. Grillo, S. D'Agostino, F. Della Sala, C. Giannini, D. Altamura, C. Oelsner, C. Kryschi and P. D. Cozzoli, *ACS Nano*, 2013, **7**, 7352-7369.
22. I. Kriegel, C. Jiang, J. Rodríguez-Fernández, R. D. Schaller, D. V. Talapin, E. da Como and J. Feldmann, *J. Am. Chem. Soc.*, 2012, **134**, 1583-1590.
23. X. Liu and M. T. Swihart, *Chem. Soc. Rev.*, 2014, **43**, 3908-3920.
24. J. M. Luther, P. K. Jain, T. Ewers and A. P. Alivisatos, *Nat. Mater.*, 2011, **10**, 361-366.
25. E. Ringe, J. M. McMahon, K. Sohn, C. Cobley, Y. Xia, J. Huang, G. C. Schatz, L. D. Marks and R. P. Van Duyne, *J. Phys. Chem. C*, 2010, **114**, 12511-12516.
26. J. Zheng, X. Cheng, H. Zhang, X. Bai, R. Ai, L. Shao and J. Wang, *Chem. Rev.*, 2021, **121**, 13342-13453.
27. C. Langhammer, M. Schwind, B. Kasemo and I. Zorić, *Nano Lett.*, 2008, **8**, 1461-1471.
28. S. Link and M. A. El-Sayed, *J. Phys. Chem. B*, 1999, **103**, 4212-4217.
29. G. V. Hartland, *Chem. Rev.*, 2011, **111**, 3858-3887.
30. S. Linic, S. Chavez and R. Elias, *Nat. Mater.*, 2021, **20**, 916-924.
31. M. Ahlawat, D. Mittal and V. Govind Rao, *Commun. Mater.*, 2021, **2**, 114.
32. L. Chen, M. Sakamoto, R. Sato and T. Teranishi, *Faraday Discuss.*, 2015, **181**, 355-364.
33. H. Li, M. Shibuta, T. Yamada, H. Hojo, H. S. Kato, T. Teranishi and M. Sakamoto, *J. Phys. Chem. C*, 2022, **126**, 8107-8112.
34. W. van der Stam, S. Gudjonsdottir, W. H. Evers and A. J. Houtepen, *J. Am. Chem. Soc.*, 2017, **139**, 13208-13217.
35. Y. Xie, A. Riedinger, M. Prato, A. Casu, A. Genovese, P. Guardia, S. Sottini, C. Sangregorio, K. Miszta, S. Ghosh, T. Pellegrino and L. Manna, *J. Am. Chem. Soc.*, 2013, **135**, 17630-17637.
36. J. Ludwig, L. An, B. Pattengale, Q. Kong, X. Zhang, P. Xi and J. Huang, *J. Phys. Chem. Lett.*, 2015, **6**, 2671-2675.
37. M. Schreck and M. Niederberger, *Chem. Mater.*, 2019, **31**, 597-618.
38. N. Zhang, D. C. J. Neo, Y. Tazawa, X. Li, H. E. Assender, R. G. Compton and A. A. R. Watt, *ACS Appl. Mater. Interfaces*, 2016, **8**, 21417-21422.
39. Y. Kim, J. Ryu, M. Park, E. S. Kim, J. M. Yoo, J. Park, J. H. Kang and B. H. Hong, *ACS Nano*, 2014, **8**, 868-874.
40. Z. Lian, M. Sakamoto, J. J. M. Vequizo, C. S. K. Ranasinghe, A. Yamakata, T. Nagai, K. Kimoto, Y. Kobayashi, N. Tamai and T. Teranishi, *J. Am. Chem. Soc.*, 2019, **141**, 2446-2450.
41. M. Huang, X. Wang, G. Xing, C. Meng, Y. Li, X. Li, L. Fan, Y. Wan and S. Yang, *J. Phys. Chem. Lett.*, 2021, **12**, 7988-7996.
42. P. R. Brown, D. Kim, R. R. Lunt, N. Zhao, M. G. Bawendi, J. C. Grossman and V. Bulović, *ACS Nano*, 2014, **8**, 5863-5872.